J Mater Sci (2017) 52:3353–3367

Macro- and micromechanical behaviors of poly(lactic acid)–hydroxyapatite electrospun composite scaffolds

F. M. Sánchez-Arévalo[1,*], L. D. Muñoz-Ramírez[1], M. Álvarez-Camacho[2], F. Rivera-Torres[3], A. Maciel-Cerda[1], R. Montiel-Campos[4], and R. Vera-Graziano[1]

[1] *Instituto de Investigaciones en Materiales, Universidad Nacional Autónoma de México, Apdo. Postal 70-360, Cd. Universitaria, 04510 México, México*

[2] *Laboratorio de Ingeniería de Rehabilitación, Instituto Nacional de Rehabilitación, Luis Guillermo Ibarra Ibarra, Av. México Xochimilco 289, Col. Arenal deGuadalupe, 14389 México, México*

[3] *Depto. de Física y Química Teórica, Lab. Física. Facultad de Química, Universidad Nacional Autónoma de México, Apdo. Postal 70-360, Cd. Universitaria, 04510 México, México*

[4] *Depto. Física Av. San Rafael Atlixco, Universidad Autónoma Metropolitana-Iztapalapa, Av. San RafaelAtlixco 186 Col. Vicentina, Iztapalapa, 09340 México, México*

Received: 14 October 2016
Accepted: 18 November 2016
Published online: 28 November 2016

ABSTRACT

It was demonstrated that the macro- and micromechanical behaviors of electrospun composite scaffolds based on PLA and HA can be simultaneously studied using 3D digital image correlation strain measurements coupled with an axial tensile test. It was proven that the addition of a small quantity (2%) of HA particles into PLA electrospun scaffolds decreased their mechanical properties by approximately 40 and 60% at the micro- and macroscales, respectively; nevertheless, when this amount was increased beyond 2% of HA, the composites recovered their stiffness, showing Young's moduli ranging between 400 and 600 MPa. Hence, the mechanical responses of PLA–4% HA and PLA–6% HA electrospun scaffolds were conveniently enhanced with the addition of hydroxyapatite nanoparticles. The micromechanical measurements were able to capture the microstrain mechanism between electrospun nanofibers and the effect of HA nanoparticles on their mechanical response. This methodology could be a powerful tool for developing scaffolds for specific applications in tissue engineering.

Introduction

According to the organ procedure transplant network (OPTN) and the Scientific Registry of Transplant Recipients (SRTR) databases (USA, March 13, 2015), approximately 134,621 persons require a lifesaving organ transplant [1]; some of them will die each day while waiting for one. Although the number of donors has increased [2], up to 30% of removed organs are discarded, primarily due to their poor quality tissue; in addition to this issue, the host often presents complications, such as infections or even rejection of the tissue/organ after

Address correspondence to E-mail: fsanchez@iim.unam.mx

DOI 10.1007/s10853-016-0624-y

transplantation. To address this problem, tissue engineering and materials science are focused on developing new materials and techniques that allow for the satisfactory replacement of native tissue [3–5].

A common strategy in tissue engineering is the use of biodegradable biomaterials to mimic the basic functions of native tissues; therefore, the scaffolds should be viewed as an artificial extracellular matrix (biomimetic structures) whose main objectives are as follows: (a) define a space to mold a regenerative tissue, (b) temporarily substitute tissue functions, (c) guide the tissue ingrowth, and (d) promote cell growth and native extracellular matrix generation [6, 7].

To produce appropriate scaffolds, several techniques have been used, such as particulate leaching, gas foaming, fiber networking, phase separation, melt molding, emulsion freeze drying, solution casting, freeze drying, electrospinning, 3D printing and, in other cases, a combination of these techniques [5, 7, 8].

The electrospinning technique has been demonstrated to be a promising technique for developing scaffolds for different purposes, including tissue engineering; this technique has also been used for localized drug delivery and promoting wound healing, among others [9–17]. Despite the aforementioned potential, the application of electrospun nanofibers has been limited due to the difficulties in mass production and the lack of knowledge of mechanical properties at that scale. This is why there is a special interest in knowing the structural, electrical, mechanical, and thermal properties of electrospun PLA fibers [18].

Some efforts have been focused on understanding the mechanical response of collagen fiber networks considering theoretical aspects from a micromechanics perspective [19, 20]. Other authors have focused their efforts on solutions for describing the elastic behavior of a spherical particle or cylindrical fibers with a homogeneous interphase [21–23]. More recently, mathematical models based on homogenization and on the differential replacement method (DRM) have been developed to predict the elastic response of poly(lactic acid) (PLA) electrospun nanofiber scaffolds [24]. In the work of Gomez-Pachon et al., experimental data and theoretical models were used to obtain the elastic modulus of PLA electrospun nanofibers, and they found a strong correlation between the electrospinning parameters, microstructure, and mechanical behavior; nevertheless, this work only reported the macromechanical behavior, obtained experimentally, for the electrospun nanofiber mats [24].

To understand the mechanical behavior of nanofibers, experimental devices and novel techniques have been developed to conduct micro-/nanoscale tension measurements in individual nanofibers [25]. The measurements showed that nanofibers are highly susceptible to surface processes that regulate their load-bearing capability and mechanics; this leads to particular behaviors that are not encountered at macroscale levels.

Although there are several reports that attempt to explain the mechanical response of electrospun nanofibers, there is a lack of knowledge on the micromechanical response of PLA–HA electrospun nanofiber composite scaffolds. The aim of this work was to evaluate the macro- and micromechanical behaviors of PLA and PLA–HA electrospun nanofiber composite scaffolds under uniaxial tension using a 3D digital image correlation technique coupled with the mechanical testing machine.

Hence, correlating the composition, structure, and macro- and micromechanical responses of electrospun nanofiber scaffolds will permit a better understanding of these materials to manipulate their properties according to the application in which the scaffold would be used. Nevertheless, at this point, there are questions that have to be answered. How do the HA particles work? Do they work as a filler that improves the mechanical and biological responses or as an inclusion that improves the biological response but decreases mechanical properties? To answer these questions, macro- and micromechanical analyses have to be conducted. In the case of scaffolds or soft biological materials with reduced thicknesses, it is not possible to hang a mechanical extensometer or bond an electrical strain gage to obtain a reliable strain measurement; furthermore, a non-contact technique to measure strain has to be used. In this work, 3D digital image correlation (DIC) analysis was coupled with the uniaxial tensile test to correlate the macro- and micromechanical responses of PLA and PLA–HA electrospun nanofiber composite scaffolds.

Experimental details

Materials and methods

Materials

Nanofiber composite scaffolds of poly(lactic acid) and 2, 4, and 6 wt% of hydroxyapatite (HA) were

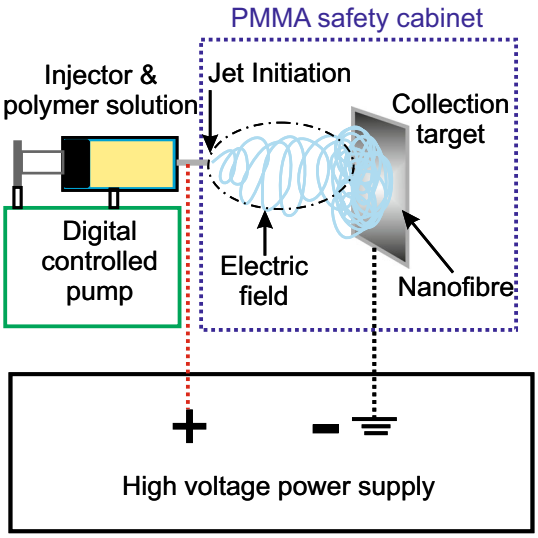

Figure 1 Experimental setup for electrospinning process to produce composite nanofiber scaffolds using polymeric solutions of PLA and PLA–HA.

obtained by electrospinning. PLA (M_w 230000, NatureWorks 2002D LLC, MN, USA) and the HA particles (diameter ≤200 nm, Sigma Aldrich) were used as received. The PLA was dissolved in 2,2,2-trifluoroethanol (Sigma Aldrich) under magnetic stirring to obtain a 16% (w/v) PLA solution. The HA particles were added to the previous mixture and then magnetically stirred to obtain the PLA–HA solutions. Both the PLA and PLA–HA solutions were separately electrospun to obtain randomly oriented nanofiber scaffolds of PLA and PLA–HA by using a 10-cm square aluminum plate as a collector. The electrospinning process was performed at room temperature and pressure at a flow rate of 0.6 ml/h (using a digitally controlled injector, KD Scientific, USA) with an applied voltage of 15 kV (power supply, Spellman, USA; the scheme in Fig. 1 depicts the electrospinning setup).

Methods: structural, thermal, and mechanical characterization

Scanning electron microscopy (SEM)

The morphology and distribution of the randomly oriented nanofibers were observed using a JEOL JSM-7600F microscope. The operating voltage of the electron beam was 20 kV. The samples were previously coated by sputtering with gold using a current of 30 mA for 3 min to increase the conductivity of the surface fibers. ImageJ software was used to measure the average diameter of the nanofibers by digital image processing. The diameters of the continuous fibers located at the foreground plane of the micrograph were measured. For the statistical analysis, several diameters of interest of nanofibers were measured. From this, the average diameter and its standard deviation are obtained. In addition, the SEM images were also used to determine the foreground porosities of the scaffolds through digital image analysis performed using ImageJ software. The images were binarized to distinguish the holes from the fibers, and then the percentages of the image corresponding to fibers and holes were calculated within an area of 11.3 × 8.5 μm^2.

Differential scanning calorimetry (DSC)

The thermal transitions in the nanofibers were determined using DSC (2910, TA Instruments). The scaffolds obtained by electrospinning were cut using a circular jig to obtain samples with a diameter of 0.5 cm; the samples were encapsulated in an aluminum standard pan. The samples were heated from 0 to 180 °C at a heating rate of 10 °C/min. The thermograms were analyzed using TA Instruments Universal Analysis 2000 software.

Fourier transform infrared (FTIR) spectroscopy

The electrospun scaffolds obtained as mats (thickness 90–200 μm) were characterized using FTIR spectroscopy to find the polymer chemical groups and the possible interactions of PLA–HA and PLA–HA with the paint that is necessary for surface preparation for further mechanical analysis by digital image correlation. Attenuated total reflectance (ATR) FTIR spectroscopy was performed using a Spectrum GX spectrometer (Perkin-Elmer, USA). The FTIR spectra were normalized, and the major vibrational bands were identified and associated with their chemical groups.

Macromechanical characterization

For the mechanical tensile tests, the samples were cut using a die according to the ASTM D1708 standard (see Fig. 2a). The thicknesses of the samples were measured using a Mitutoyo digimatic micrometer, model 293-67N. The width of the samples was 5 mm,

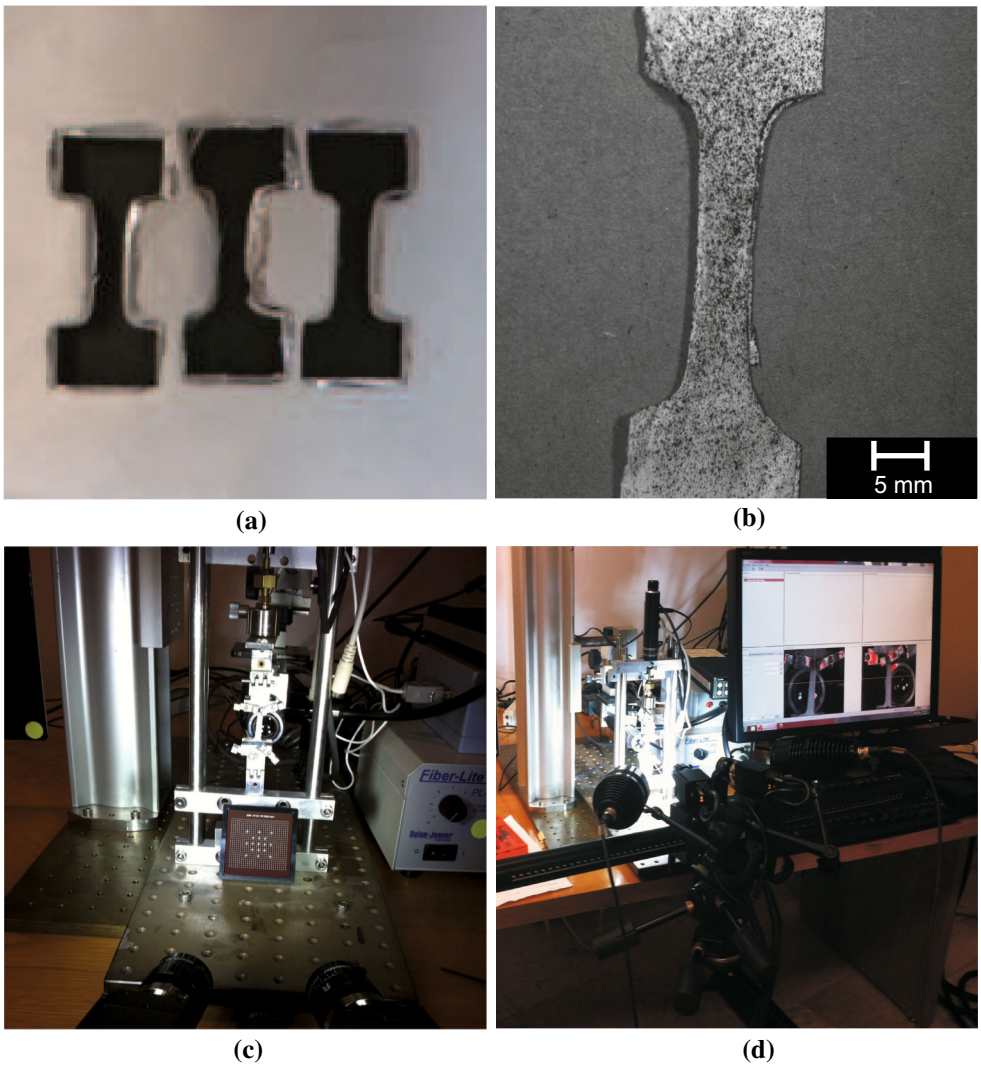

Figure 2 Experimental setup for macro- and micromechanical measurements of PLA and PLA–HA electrospun scaffolds. **a** Tensile samples cut from electrospun scaffolds, **b** tensile sample prepared for non-contact strain measurement, **c** custom-designed minitester to determine the mechanical response of soft materials and **d** complete experimental setup to correlate the macro- and micromechanical responses of PLA and PLA–HA electrospun scaffolds.

as shown in Fig. 2b. Hence, knowing the sample dimensions (width and thickness) and their porosities, the porous cross-sectional areas (A_p) of the samples were easily determined, as previously mentioned in the morphology section. The mechanical tensile tests were conducted using a custom-designed minitester that was developed previously [26]. This micromechanical tester is based on a load frame designed to apply uniaxial load on soft and thin material samples, as shown in Fig. 2c. The uniaxial tensile tests were conducted using a cross-head speed of 0.16 mm/s; the sample dimensions were 38, 5, and 0.125 mm (length, width, and thickness, respectively), and the equivalent length was $l_0 = 22.2$ mm.

The stress as a function of strain curve was obtained considering the porous cross-sectional area (A_p) of the sample and the equivalent distance (l_0) between grips; hence, the macromechanical response based on the stress and strain engineering curve can be determined using the following expressions: $\sigma = \frac{F}{A_p}$ and $\varepsilon = \frac{\Delta l}{l_0}$, where F is the registered force during the tensile test and (A_p) is calculated using the solid cross-sectional area multiplied by the average porosity value of the electrospun scaffold; Δl are the increments of displacement registered during the tensile test and l_0 is the initial distance between the grips. The constitutive model is the uniaxial case of

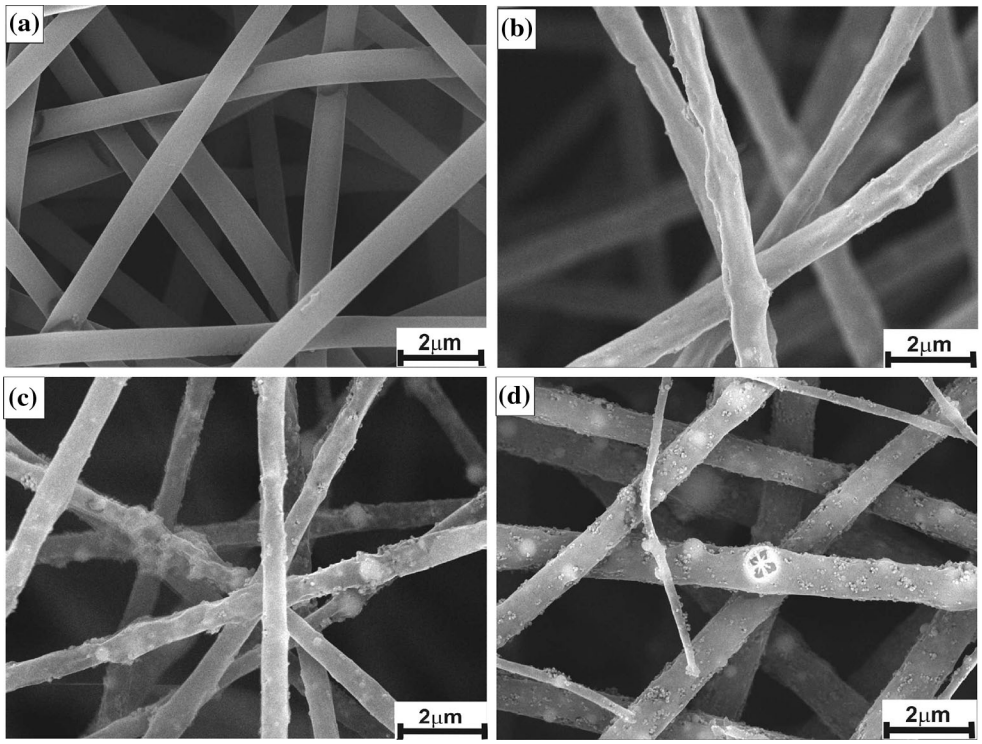

Figure 3 Morphological changes of PLA scaffolds as a function of HA concentration evaluated by scanning electron microscopy: **a** Pure PLA fibers, **b** PLA–2% HA particles completely embedded in the fiber, **c** PLA–4% HA, and **d** PLA–6% HA.

Hooke's law ($\sigma = E * \varepsilon$), where E is the Young's modulus.

From the acquired data, it was possible to calculate the curve of stress as a function of strain for the electrospun nanofiber scaffolds. From these curves, the Young's modulus was determined for each sample, taking into account the slope of the stress vs. strain curve in the linear region.

All relevant parameters for this test, such as time, load, and displacement, were monitored via electronic sensors; in addition to the standard uniaxial tensile experiment setup, a non-contact method for full-field strain measurements was coupled to correlate the macro- and micromechanical responses of the electrospun scaffolds.

Micromechanical characterization

The micromechanical characterization was performed by coupling the uniaxial tensile minitester with a 3D image acquisition ARAMIS 5L system (Gom; Optical Measurements Techniques; Germany) [27], as shown in Fig. 2d. The ARAMIS 5L system is a non-contact optical 3D measuring system for registering, analyzing, and reporting material deformation at the micromechanical level through a 2D or 3D digital image correlation [27]. The ARAMIS 5L system uses two CCD cameras and 35 mm family B lenses to obtain a field of view of 35 × 29 mm. These lenses require a measuring distance of 215 mm and an adequate aperture, which will depend on the illumination conditions and depth of field [27]. To obtain a reliable strain measurement, the angle between the cameras for this configuration must be set at 25 degrees, according to the calibration protocol [27]. To minimize the error during the correlation process, the CCD cameras were calibrated following the protocol established in the ARAMIS 5L user manual (Gom, Optical Measurements Techniques). Data acquisition and image capture (ARAMIS 5L system) during the tensile test were conveniently synchronized with a virtual instrument specially programmed in LabVIEW software.

It is well known that some strain measurements with DIC require random speckle patterns to improve the correlation process [28]. Several works commonly use sprayed black paint over a white-painted surface; this offers a good contrast to improve the correlation process. In our case, the fibers of the electrospun scaffolds are white; therefore, black acrylic paint

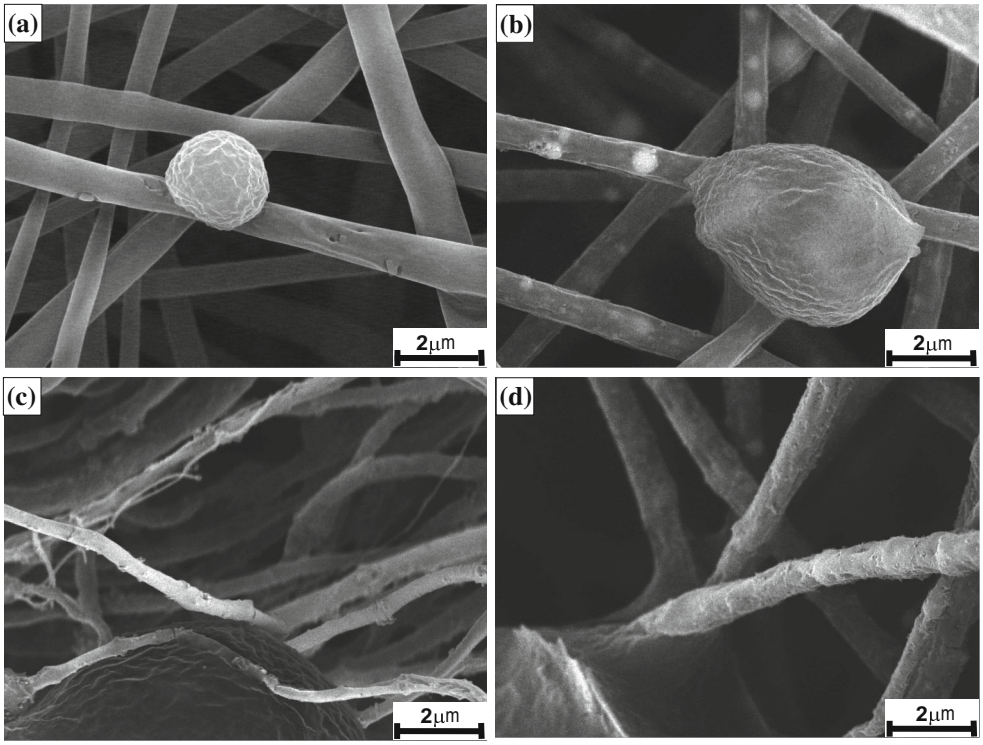

Figure 4 Sprayed drops of *black* acrylic paint on PLA and PLA–HA electrospun scaffolds. **a** Pure PLA, **b** PLA–2% HA, **c** PLA–4% HA, and **d** PLA–6% HA.

(Politec; México) was randomly sprayed on the electrospun fibers to obtain the adequate speckle pattern (see Fig. 2b). The size and distribution of the black dot pattern were selected according to the sample preparation patterns reported in the ARAMIS 5L sample preparation manual [27]. Once the random speckle pattern of acrylic paint was applied on the surfaces of the samples, a new question arose. Are there chemical interactions between the black paint and PLA–HA scaffolds or are only van der Waals forces present between the black paint and scaffolds? This issue will be answered by FTIR analysis.

As previously mentioned, our analysis was focused on the linear region of the stress vs. strain curve; therefore, time, force, and displacement data were synchronized with the image acquisition system (3D ARAMIS 5L) during the tensile test. The microstrain measurements were calculated using the von Mises criterion, which are available in the ARAMIS 5L software [27]. Hence, the principal strains and their directions were easily obtained. Finally, both the macro- and micromechanical responses of the electrospun nanofiber scaffolds can be correlated. This analysis registered the evolution of the strain concentration as a function of the position on the working section of the sample for different stress values.

Results and discussion

Morphology by scanning electron microscopy (SEM)

SEM micrographs of the PLA and PLA–HA electrospun nanofibers scaffolds are shown in Fig. 3. These four micrographs show the morphology of the PLA randomly oriented electrospun fibers. Figure 3a corresponds to pure PLA; the next three micrographs (Fig. 3b–d) correspond to PLA with 2, 4, and 6% by weight of hydroxyapatite (HA) particles, respectively. Note that all of the PLA electrospun scaffolds were collected under the same conditions, as described in "Materials" section; therefore, we assumed that the addition of HA particles modified the morphology of the fibers. Figure 3a shows the pure PLA fibers with a smooth surface and homogeneous diameters (0.79 ± 0.2 μm); the addition of 2% HA particles to the PLA (Fig. 3b) caused several

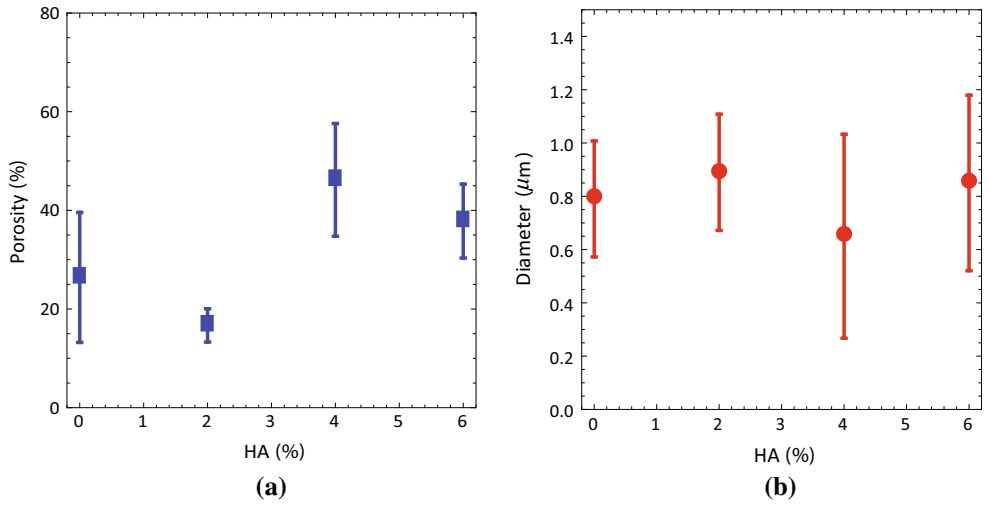

Figure 5 Quantification of morphological parameters of the electrospun scaffolds as a function of HA content. **a** Porosity and **b** diameter.

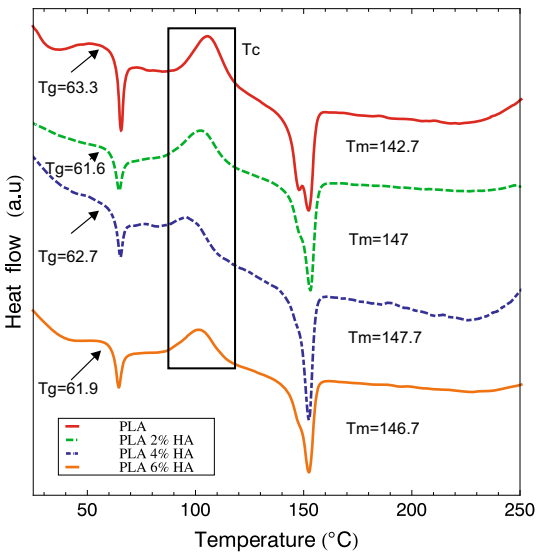

Figure 6 Thermal transition temperatures of PLA and PLA–HA electrospun scaffolds as a function of HA content.

irregularities in the shape of the fiber; the diameters of the fibers were (0.89 ± 0.2 μm). Increasing the HA content to 4% (Fig. 3c) caused the fibers to recover their homogeneity in shape with diameters of 0.65 ± 0.3 μm. The HA particles saturated the interior of the fiber and began to appear in the fiber surface as bright spots; finally, Fig. 3d corresponds to PLA–6% HA scaffold. Here, the shape uniformity of the fibers was observed again; note that similar diameters for pure PLA and PLA–6% HA scaffolds were obtained (0.85 ± 0.3 μm).

Figure 4 presents the SEM images of the scaffolds where the random speckle pattern with paint was applied. In these images, black drops of paint presented high contact angles (124 ± 10 °C), and curly spherical surfaces are shown; this means that water evaporation occurred during the polymerization process of the acrylic paint. The high contact angles of the paint drops suggest that only van der Waals forces are present between the PLA fibers and acrylic paint. Note that the porosity and the average diameter of fibers of the scaffolds on the foreground were determined from the SEM images using digital image analysis.

The percentage of porosity and the diameter of the fibers as a function of HA particle concentration are presented in Fig. 5a, b. The porosity values ranged between 20 and 50%, and the diameter of the fibers ranged between 600 and 850 nm. Hence, increasing the HA content modified the porosity of the scaffolds until it was two times greater (see Fig. 5a); in the case of the diameters, it was found that the HA content increased the dispersion of average diameters, which means that variability in the mechanical properties will be expected.

Thermal transitions by differential scanning calorimetry (DSC)

The thermal transitions of the PLA and PLA–HA electrospun scaffolds were studied using DSC to analyze any trends in crystallization; the thermal transitions of the electrospun scaffolds are shown in Fig. 6. The glass transition (T_g = 60–63 °C) and melting (T_m = 142–147 °C) temperatures were approximately equal in all cases, as previously

Table 1 Thermal transition temperatures and their associated enthalpies for PLA and PLA–HA electrospun scaffolds

Samples	T_g (°C)	H_{T_g} (J/g)	T_c (°C)	H_{T_c} (J/g)	T_m (°C)	H_{T_m} (J/g)
PLA	63.3	6.05	91.4	17.3	142.7	20.8
PLA–2% HA	61.6	5.74	85.8	10.7	147	18.7
PLA–4% HA	62.7	6.04	81.2	7.1	147.7	19.0
PLA–6% HA	61.9	5.03	82.2	12.2	146.7	18.4

reported [29]; nevertheless, the crystallization temperatures (T_c) showed changes ranging from 81 to 91 °C. This result indicates that T_c decreases with the increase in HA particles, which may be due to the HA addition and the environmental/collection conditions [24]. The thermal transition temperatures and their associated enthalpy of PLA and PLA–HA are summarized in Table 1.

All samples showed an enthalpic relaxation due to the solidification rate during the electrospinning process. This enthalpic relaxation temperature began at approximately 64 °C (endothermic peak). The degree of molecular disorder of the chains is associated with the enthalpy of this peak. From the enthalpic relaxation values (Table 1), we can state that the molecular disorder of the chains of these electrospun scaffolds (both composed of pure PLA and PLA–HA) is almost identical. As shown in Fig. 6, the PLA and PLA–HA scaffolds exhibited exothermic peaks between 81 and 91 °C. These peaks, with enthalpy values ranging between 7.1 and 17.3 J/g, show that the crystallization trend of the polymer decreased when HA particles were added. The energy released during crystallization was higher in PLA than in the blends of PLA–HA. The melting point was observed at approximately 138–142 °C. Again, the melting peak of the PLA was more intense than those of PLA–HA blends, with enthalpies ranging between 18.4 and 20.8 J/g, indicating a greater crystalline fraction in the pure PLA electrospun scaffolds.

Chemical analysis by Fourier transform infrared (FTIR) spectroscopy

Once the random speckle pattern of acrylic paint was applied onto the surfaces of the samples, a new question arose. Are there chemical interactions between the black paint and PLA–HA scaffolds or are there only van der Waals forces present between the black paint and scaffolds? To answer this question, we have to consider that the electrospun scaffolds are primarily composed of PLA; therefore, possible chemical interactions might be present between PLA and acrylic paint molecules, as shown in Fig. 7a. The scheme in Fig. 7b depicts the electrospun PLA fibers with HA and PLA fibers with HA and the acrylic black paint sprayed on the fibers; this scheme shows the evaporation process of the paint solvents: in stage 1, a drop of acrylic paint mixed with water is located on the PLA–HA fiber; subsequently, water evaporation occurs, producing a drop contraction. Stage 2 illustrates a dried drop of black paint adhered to the fiber. Finally, when the solvents, mainly water, evaporate, the random dots of paint are obtained. After the evaporation of the solvents, the remaining components of the acrylic paint become in direct contact with the electrospun fibers. With this closer contact emerges the possibility of chemical reactions among the PLA of the electrospun fibers and the poly(ethyl acrylate), PEA, of the acrylic resin of the paint and with the HA particles, as well. However, the required conditions for the chemical reactions were not present, and this is discussed as follows: the possible free radical reaction between PLA and PEA requires a catalytic action; a possible source of free radicals are those remaining from the polymerization reaction to produce the PEA. Normally, they are deactivated at the end of the reaction. On the other side, fillers of paint may act like a photocatalyst when they contain TiO_2 and are exposed to sun light, particularly near-UV and Vis range [30]; however, a photocatalytic action from the fillers of this black paint is not expected according to its composition. An X-ray analysis revealed the following constituents: magnesite (46%), anthophyllite (38%), and nimite (16%). The magnesite ($MgCO_3$) is very stable at room temperature, and its thermal modification begins at approximately 640 °C [31]. Anthophyllite and nimite are the aluminum silicates that are also very stable at room temperature. Furthermore, there are currently no reports in the literature of photocatalytic activity for any of the three fillers, in contrast to TiO_2. A

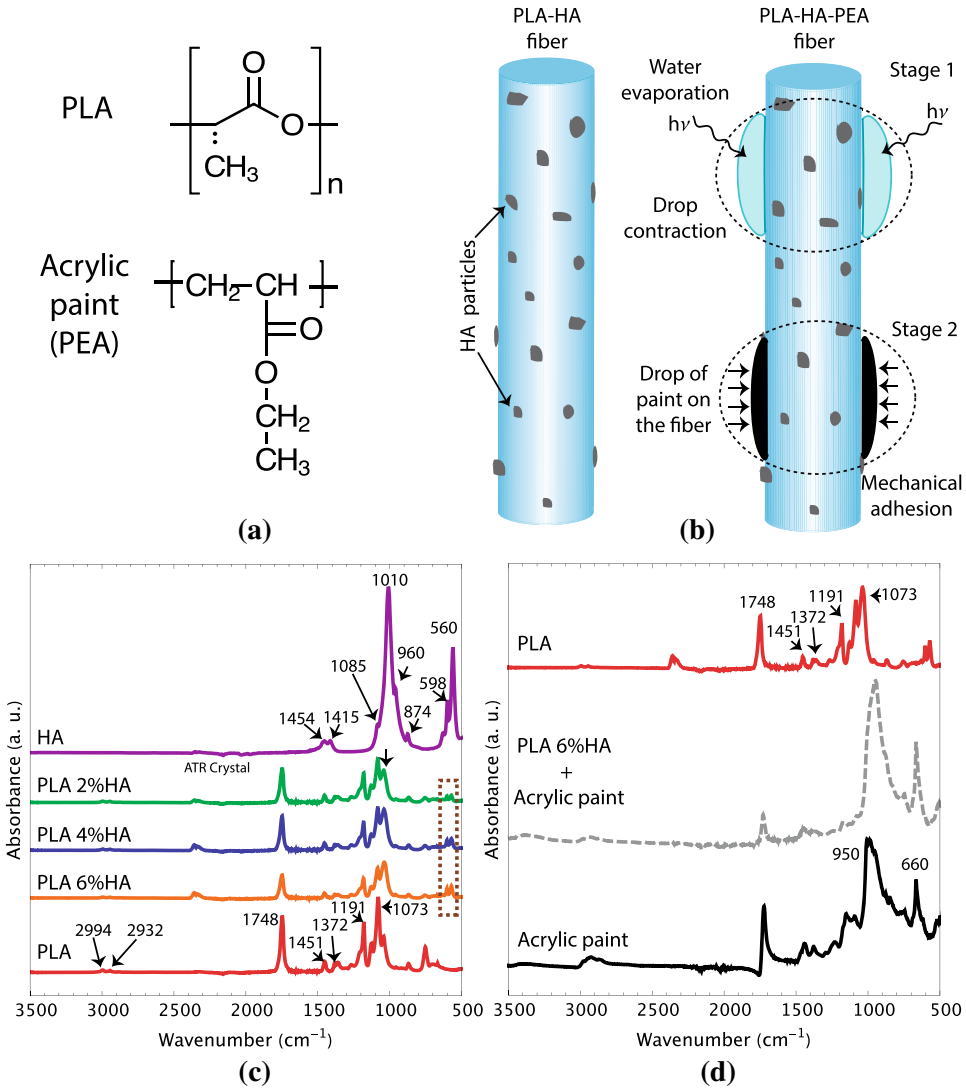

Figure 7 **a** Molecules of PLA and acrylic paint that interact during the sample preparation for DIC, **b** scheme of black paint drop formation on PLA fibers, **c** interaction of functional groups of PLA and HA determined by FTIR and **d** functional group interactions among PLA, HA, and *black* acrylic paint.

transesterification reaction between PLA and PEA would require an alkoxide or a coordination catalyst and a temperature above 100 °C. The grafting reaction of PLA–HA onto PEA of the acrylic resin was discarded because the required temperature to initiate this reaction is 120 °C in the presence of an appropriate catalyst [32]. Note that in our samples, the acrylic paint was sprayed at room temperature.

Figure 7c shows the FTIR spectra for the electrospun fibers of pure PLA (bottom spectra) and pure HA (top spectra). In the middle of them, the spectra of PLA–HA blends containing 2, 4, and 6% of HA particles are shown. Table 2 presents the peak assignments for the raw materials and their blends. The FTIR spectra for PLA were in excellent agreement with those previously reported in the literature [33, 34]. Some similarity between the FTIR spectra of PLA and PAE [35] is expected because of the coincidence in functional groups in both polymers that can be observed from the infrared spectra: C=O, C–O, CH_3, and CH. The only structural difference between both polymers is that PAE has two CH_2 and PLA does not contain this group. Therefore, the signals from the analysis of the FTIR spectra for PLA and PAE are quite similar and are reported in Table 2; however, the PAE signals appear shifted to lower wavelengths compared to the PLA signals. Most of the spectra of the blends of PLA and HA painted with the acrylic paint are the arithmetic sum of all the components. Thus, infrared spectroscopy confirmed that there is no chemical reaction between the electrospun fibers and the sprayed acrylic black paint. The entire signals for CH_3 are assigned as follows: for the asymmetric stretching, the characteristic bands

Table 2 Functional groups of PLA, HA, PLA+HA, and acrylic paint (wavenumber cm^{-1})

Functional groups	PLA	HA	Acrylic paint	(PLA–HA) + acrylic paint
CH_3 ν_{as}	2994	–	2973	2994
CH_3 ν_s	2932	–	2911	2932
C=O ν_s	1748	–	1729	1708
CO_3^{2-}	–	1454	–	–
CO_3^{2-} ν_{group}	–	1415	–	–
CH_3 ν_{as}	1451	–	1441	1451
CH_3 ν_s	1372	–	1361	1361
O–C–O ν_{as}	1192	–	1167	1192
O–C–O ν_s	1110	–	1042	1110
P–O ν_{bend}	–	1085	–	–
CH_3–C ν_s	1073	–	1042	1073
P–O ν_{bend}	–	1010	–	–
P–O–P ν_s	–	960	–	–
CO_3^{2-} ν_{group}	–	874	–	–
–CH= ν_{as}	845	–	752	845
O–P–O ν_{bend}	–	598,569	–	–

are at 2994 and at 1451 cm^{-1}, whereas the bands for symmetric stretching are at 2932 and at 1372 cm^{-1}. The stretching band for C=O of the carbonyl group of the polymers is at approximately 1748 cm^{-1}. The C–O–C presents a band at 1192 cm^{-1} because of asymmetric stretching, whereas the symmetric stretching of this group is at 1110 cm^{-1}. The absorbance peak at 1073 is assigned to CH_3–C in its symmetric deformation. There is another band of symmetric deformation at 845 cm^{-1} assigned to C–COO. The presence of the HA in PLA fibers was first confirmed by SEM images, and now it is confirmed by FTIR analysis. The characteristic peaks for the HA [36] are for the CO_3^{2-} group at 1415 and 1454 cm^{-1} . There is another deformation band assigned to the the asymmetric stretching, the characteristic bands CO_3^{2-} group at 874 cm^{-1} . The phosphorous and its links with oxygen gives several bands, including two bending bands at 1085 and 1010 cm^{-1} assigned to P–O. For P–O–P, there is a band of stretching deformation at 960 cm^{-1} . Finally, two bands of bending are at 560 and 598 cm^{-1}, both assigned to PO_4^{3-}. These results have also been observed for HA by other authors [36]. From the FTIR analyses, we can conclude that there are no chemical reactions in the adhesion process of the black paint and PLA with HA nanofibers when black acrylic paint is used to obtain a random speckle pattern. Furthermore, its use on PLA–HA scaffolds does not affect their mechanical response. Thus, typical sample preparation for the digital image correlation (DIC) technique can conveniently be used to evaluate the micromechanical behavior of PLA–HA-based scaffolds.

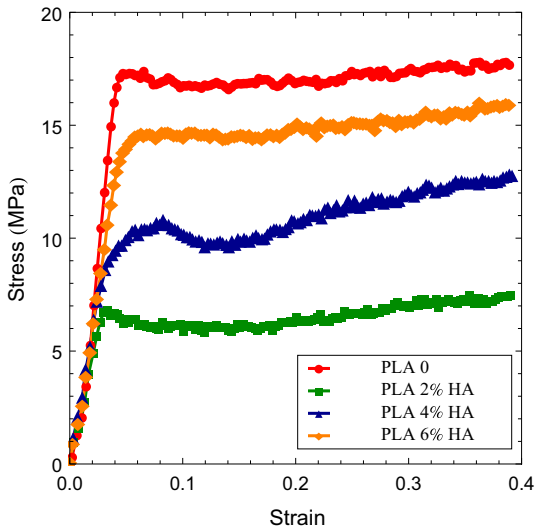

Figure 8 Macromechanical response of PLA and PLA–HA scaffolds showing the influence of the embedded HA particles.

Macromechanical characterization

The mechanical behaviors of the PLA and PLA–HA electrospun scaffolds are presented in Fig. 8. This figure shows the representative stress versus strain curves where the macromechanical responses of the

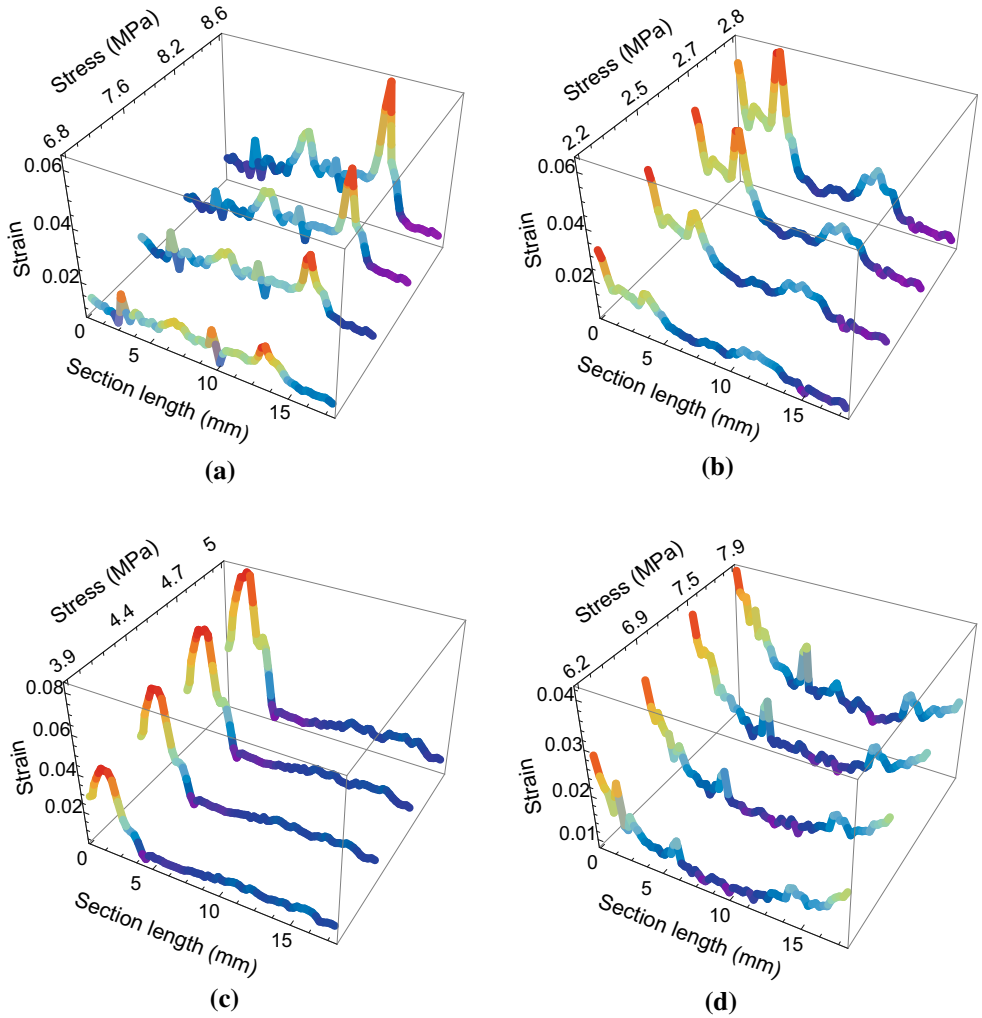

Figure 9 Micromechanical behavior of PLA before yielding showing the evolution of the stress and microstrain concentration of the PLA and PLA–HA electrospun scaffolds. **a** Pure PLA showing an intense peak of strain, located at 12 mm away from the fixed grip, between 6.8 and 8.6 MPa; **b** PLA–2% HA scaffold showing a well-defined strain peak between 2.2 and 2.8 MPa, which is located at 3 mm from the fixed grip; **c** PLA–4% HA scaffold reveals that the addition of HA particles acts as a reinforcement factor between 5 and 15 mm in section length; and **d** the PLA–6% HA sample also shows the reinforcement effect at the micromechanical level of HA particles embedded in the PLA electrospun scaffolds.

PLA and PLA–HA electrospun scaffolds are observed; it is clear that these representative curves show a linear behavior below a strain of 0.02. In addition, it can be observed that the maximum stress values before yielding for these representative curves were 17, 6.5, 10, and 14 MPa for pure PLA, PLA–2% HA, PLA–4% HA, and PLA–6% HA, respectively. The macromechanical behavior suggests that the HA particles acted as an inclusion that rapidly decreased the mechanical response of the PLA–2 % HA scaffolds. Moreover, increasing the HA content beyond 2% in the PLA scaffold showed that these particles acted as a reinforcement; furthermore, better strength and Young's moduli were observed for PLA–4% HA and PLA–6% HA than for the PLA–2 % HA scaffolds. The PLA–6% HA scaffold presented mechanical properties close to those of the pure PLA; the main advantage of PLA–6% HA might be that its biological compatibility could be higher than that of pure PLA. To summarize, the addition of small quantities, beyond 2 wt%, of HA particles enhanced the mechanical properties of the scaffold and also could promote better cellular adhesion and proliferation.

Table 3 Elastic moduli (MPa) at the macro- and micromechanical levels of PLA and PLA–HA considering the porosities of the scaffolds

Samples	E_{micro} (MPa)	E_{macro} (MPa)
PLA	581 ± 150	473 ± 55
PLA–2% HA	355 ± 104	190 ± 84
PLA–4% HA	526 ± 156	384 ± 103
PLA–6% HA	625 ± 122	395 ± 115

Micromechanical characterization

This section is concerned with the micromechanical measurements of the PLA and PLA–HA scaffolds. From the FTIR, SEM, and DSC results, we now have evidence about the interaction level between PLA, PLA–HA, and acrylic paint. It is clear that the acrylic paint interaction does not affect the micromechanical measurements with the DIC 3D technique or the mechanical behavior of the scaffolds. Figure 9 shows the evolution of strain concentration, while the load applied to the scaffolds is increased. For this analysis, we consider three cases: (i) the first only considers the main strain values for one longitudinal line of 15 mm in length located at the center of the sample; (ii) the second case considers the main average strain value of the three longitudinal lines, one line located at the center of the sample and the others located at the right and left sides of the central line; and (iii) the third case takes into account five longitudinal lines: one is located at the center of the sample, and the other four lines are located in the sample (two at the right side and two at left side of the central line; all of them equidistantly separated). The evolution of the strain concentration as a function of the position (along the sample) for different stress values is presented in Fig. 9 case (i). Here, the strain concentration effect can be observed for PLA, PLA–2% HA, PLA–4% HA, and PLA–6% HA (Fig. 9a–d, respectively). Similar curves were obtained for cases (ii) and (iii), but they are not presented. Note that the microstrain measurements revealed a heterogeneous nature of the PLA and PLA–HA scaffolds for different stress levels.

From these curves, the Young's modulus at the micromechanical level of each scaffold was calculated according to Hooke's law, where σ is the mechanical stress, ε is the average of the strain along the section length (determined by DIC analysis), and E is the Young's modulus. The Young's moduli at the macro- and micromechanical levels are summarized in Table 3.

Comparing the macromechanical and micromechanical responses, a clear trend is shown in Fig. 10. The average values of the maximum stress before yielding as a function of HA content are presented in Fig. 10a. Here, the macromechanical response of the PLA–HA samples shows that the addition of 2% of HA drastically diminished the value of the maximum stress before yielding by 54%; nevertheless, similar values of maximum stress for pure PLA (13.7 MPa)

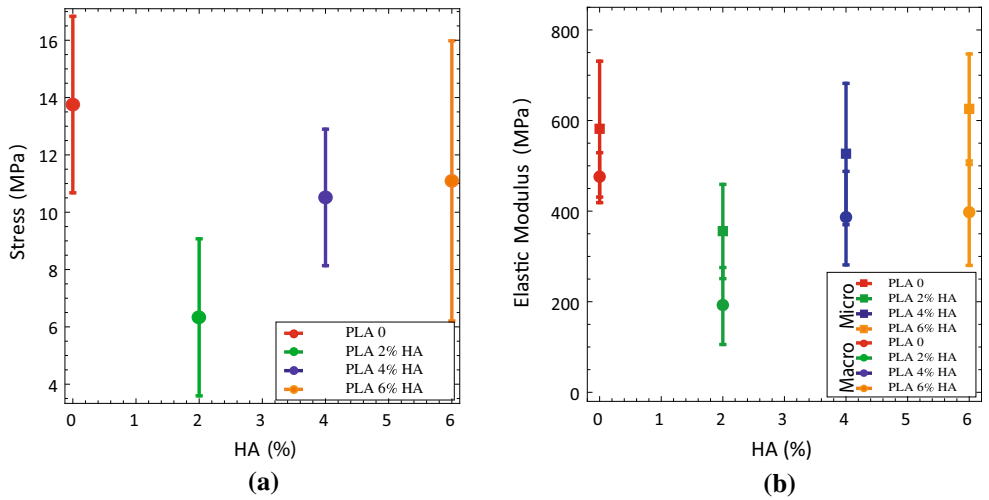

Figure 10 Macro- and micromechanical responses of PLA electrospun composite scaffolds. **a** Average of maximum stress before yielding for pure PLA and PLA–HA composites, and **b** Young's moduli at the macro- and micromechanical levels for PLA and PLA–HA electrospun composite scaffolds.

were recovered by increasing the HA% content, as shown for samples PLA–4% of HA and PLA–6 % of HA (10.5 and 11 MPa), respectively. Compared to the results reported by Xu et al. [37], we found a different trend in mechanical properties, which might due to the use of different solvents, the grade of PLA, and the electrospinning parameters when producing the PLA and PLA–HA electrospun scaffolds.

The macro- and micromechanical responses followed a similar trend, which is in good agreement with the crystallization behavior of the scaffolds detected by DSC; hence, scaffolds with a high crystalline fraction offer better mechanical properties than those with low crystallinity. The Young's modulus values at the macro- and micromechanical levels are presented in Fig. 10b. The addition of 2, 4, and 6% of HA reduced the Young's modulus at the macromechanical level as follows: 60, 18, and 16%, respectively. A similar trend was observed at the micromechanical level; the addition of 2 and 4% of HA caused a reduction in the Young's modulus as follows: 39 and 9%, respectively; nevertheless, the scaffold with 6 % of HA showed an increase of 7%.

Theoretical models such as asymptotic homogenization, laminated (E_{out}), and hierarchical models reported by Gomez-Pachon et al. [24] suggest that our electrospun scaffolds could have a laminated bimaterial periodic structure in which lamellar fractions are approximately 0.25%; hence, its Young's modulus is approximately 500 MPa. This theoretical value is in good agreement with our experimental values of Young's moduli reported in Table 3.

Conclusions

It was demonstrated that the macro- and micromechanical behaviors of electrospun composite scaffolds composed of PLA and HA can be studied and correlated using 3D digital image correlation strain measurements and uniaxial tensile tests. FTIR analysis demonstrated that the use of acrylic paint does not produce chemical bonding with the PLA–HA composite scaffolds or modify its mechanical behavior; furthermore, 3D digital image correlation strain measurements can be considered to be a powerful tool for the micromechanical characterization of scaffolds for tissue engineering. It was demonstrated that the addition of a small quantity (2%) of HA particles to the PLA electrospun scaffolds decreased their mechanical properties by approximately 40 and 60% at the micro- and macroscales, respectively; nevertheless, when increasing this amount beyond 2% of HA, the composites recovered their stiffness, showing Young's moduli ranging between 400 and 600 MPa, which is in good agreement with composite scaffolds with a laminated bimaterial periodic structure reported in the literature. Hence, the mechanical responses of the PLA–4% HA and PLA–6% HA electrospun scaffolds were conveniently enhanced with the addition of HA nanoparticles.

Acknowledgements

This work was developed with the financial support from PAPIIT DGAPA-UNAM program through Grants IT100215 and IN108116 and from CONACyT through Grants INR/UNAM-IIM/GOB-15/2014-Salud-2010-1-141036 and CNPQ117373. The authors are grateful to Dr. Omar Novelo for the FE-SEM images, Adriana Tejeda, MSc., for X-ray measurements, D. Cabrera, MSc., and E. Morales, MSc., for the DSC characterization, and Miguel Canseco, MSc., for FTIR measurements.

References

[1] OPTN/SRTR (2013) Organ Procurement and Transplantation Network (OPTN) and Scientific Registry of Transplant Recipients (SRTR) optn/srtr 2013 annual data report. Accessed 19 Mar 2015

[2] Israni AK, Zaun DA, Rosendale JD, Snyder JJ, Kasiske BL (2015) OPTN/SRTR 2013 Annual data report: deceased organ donation. Am J Transplant 15(S2):1

[3] Billiet T, Vandenhaute M, Schelfhout J, Vlierberghe SV, Dubruel P (2012) A review of trends and limitations in hydrogel-rapid prototyping for tissue engineering. Biomaterials 33(26):6020

[4] Liao S, Murugan R, Chan CK, Ramakrishna S (2008) Processing nanoengineered scaffolds through electrospinning and mineralization suitable for biomimetic bone tissue engineering. J Mech Behav Biomed Mater 1(3):252

[5] Barnes CP, Sell SA, Boland ED, Simpson DG, Bowlin GL (2007) Nanofiber technology: designing the next generation of tissue engineering scaffolds. Adv Drug Deliv Rev 59(14):1413

[6] Peltola SM, Melches FP, Grijpma DW, Kellomaki M (2008) A review of rapid prototyping techniques for tissue engineering purposes. Ann Med 40(4):268

[7] Yeong WY, Chua CK, Leong KF, Chandrasekaran M (2004) Rapid prototyping in tissue engineering: challenges and potential. Trends Biotechnol 22(12):643

[8] Lee JY, Choi B, Wu B, Lee M (2013) Customized biomimetic scaffolds created by indirect three-dimensional printing for tissue engineering. Biofabrication 5(4):045003

[9] Goh YF, Shakir I, Hussain R (2013) Electrospun fibers for tissue engineering, drug delivery, and wound dressing. J Mater Sci 48(8):3027–3054. doi:10.1007/s10853-013-7145-8

[10] Nguyen TTT, Ghosh C, Hwang SG, Tran LD, Park JS (2013) Characteristics of curcumin-loaded poly (lactic acid) nanofibers for wound healing. J Mater Sci 48(20):7125–7133. doi:10.1007/s10853-013-7527-y

[11] Choi J, Kim H, Yoo H (2015) Electrospinning strategies of drug-incorporated nanofibrous mats for wound recovery. Drug Deliv Transl Res 5(2):137–145

[12] Jin G, Prabhakaran MP, Nadappuram BP, Singh G, Kai D, Ramakrishna S (2012) Electrospun Poly(L-Lactic Acid)-co-Poly(-Caprolactone) nanofibres containing silver nanoparticles for skin-tissue engineering. J Biomater Sci Polym Ed 23(18):2337–2352

[13] Meinel AJ, Germershaus O, Luhmann T, Merkle HP, Meinel L (2012) Electrospun matrices for localized drug delivery: current technologies and selected biomedical applications. Eur J Pharm Biopharm 81(1):1–13

[14] Rieger KA, Birch NP, Schiffman JD (2013) Designing electrospun nanofiber mats to promote wound healing—a review. J Mater Chem B 1:4531–4541

[15] Kim BS, Kim IS (2011) Recent nanofiber technologies. Polym Rev 51(3):235–238

[16] Villarreal-Gómez LJ, Cornejo-Bravo JM, Vera-Graziano R, Grande D (2016) Electrospinning as a powerful technique for biomedical applications: a critically selected survey. J Bio-mater Sci Polymer Ed 27(2):157–176

[17] Honarbakhsh S, Pourdeyhimi B (2011) Scaffolds for drug delivery, part I: electrospun porous poly(lactic acid) and poly(lactic acid)/poly(ethylene oxide) hybrid scaffolds. J Mater Sci 46(9):2874–2881. doi:10.1007/s10853-010-5161-5

[18] Picciani PHS, Medeiros ES, Pan Z, Wood DF, Orts WJ, Mattoso LHC, Soares BG (2010) Structural, electrical, mechanical, and thermal properties of electrospun poly(lactic acid)/polyaniline blend fibers. Macromol Mater Eng 295(7):618–627

[19] Stein AM, Vader DA, Weitz DA, Sander LM (2011) The micromechanics of three-dimensional collagen-I gels. Complexity 16(4):22–28

[20] Stylianopoulos T, Bashur CA, Goldstein AS, Guelcher SA, Barocas VH (2008) Computational predictions of the tensile properties of electrospun fibre meshes: effect of fibre diameter and fibre orientation. J Mech Behav Biomed Mater 1(4):326–335

[21] Hori M, Nemat-Nasser S (1999) On two micromechanics theories for determining micro–macro relations in heterogeneous solids. Mech Mater 31(10):667–682

[22] Hill R (1965) A self-consistent mechanics of composite materials. J Mech Phys Solids 13(4):213–222

[23] Hashin Z, Rosen B (1964) The elastic moduli of fiber-reinforced materials. J Appl Mech 31(1):223–232

[24] Gómez-Pachón EY, Sánchez-Arévalo FM, Sabina FJ, Maciel-Cerda A, Campos RM, Batina N, Morales-Reyes I, Vera-Graziano R (2013) Characterisation and modelling of the elastic properties of poly(lactic acid) nanofibre scaffolds. J Mater Sci 48(23):8308–8319. doi:10.1007/s10853-013-7644-7

[25] Kolluru PV, Chasiotis I (2015) Interplay of molecular and specimen length scales in the large deformation mechanical behavior of polystyrene nanofibers. Polymer 56:507–515

[26] Briones-Herrera JC, Cuando-Espitia N, Sanchez-Arevalo FM, Hernandez-Cordero J (2013) Evaluation of mechanical behavior of soft tissue by means of random laser emission. Rev Sci Instrum 84(10):104301

[27] GOM (2009) GOM, Aramis User Manual Software, Optical measurements techniques p 129

[28] Haddadi H, Belhabib S (2008) Use of rigid-body motion for the investigation and estimation of the measurement errors related to digital image correlation technique. Opt Lasers Eng 46(2):185–196

[29] Solarski S, Ferreira M, Devaux E (2005) Characterization of the thermal properties of PLA fibers by modulated differential scanning calorimetry. Polymer 46(25):11187–11192

[30] Veres A, Menesi J, Juhesz A, Berkesi O, Abraham N, Bohus G, Oszko A, Potari G, Buzas N, Janovak L, Dekany I (2014) Photocatalytic performance of silver-modified TiO2 embedded in poly (ethyl-acrylate-co-methyl metacrylate) matrix. Colloid Polym Sci 292(1):207–217

[31] Hartman M, Svoboda K (1985) Photocatalytic performance of silver-modified TiO2 embedded in poly(ethyl-acrylate-co-methyl metacrylate) matrix. Ind Eng Chem Process Des Dev 24(3):613

[32] Hong Z, Qiu X, Sun J, Deng M, Chen X, Jing X (2004) Grafting polymerization of l-lactide on the surface of hydroxyapatite nano-crystals. Polymer 45(19):6699–6706

[33] Zhang J, Duan Y, Sato H, Tsuji H, Noda I, Yan S, Ozaki Y (2005) Crystal modifications and thermal behavior of poly (l-lactic acid) revealed by infrared spectroscopy. Macromolecules 38(19):8012–8021

[34] Kister G, Cassanas G, Vert M (1998) Effects of morphology, conformation and configuration on the IR and Raman spectra of various poly(lactic acid)s. Polymer 39(2):267–273

[35] del Real A, Wallander D, Maciel A, Cedillo G, Loza H (2015) Graft copolymerization of ethyl acrylate onto tamarind kernel powder, and evaluation of its biodegradability. Carbohydr Polym 117:11–18

[36] Panda R, Hsieh M, Chung R, Chin T (2003) FTIR, XRD, SEM and solid state NMR investigations of carbonate-containing hydroxyapatite nano-particles synthesized by hydroxide-gel technique. J Phys Chem Solids 64(2):193–199

[37] Xu X, Chen X, Liu A, Hong Z, Jing X (2007) Electrospun poly (l-lactide)-grafted hydroxyapatite/poly(l-lactide) nanocomposite fibers. Eur Polym J 43(8):3187–3196